Experimental Mechanics (2008) 48:403–419
DOI 10.1007/s11340-007-9084-2

Stress Reconstruction and Constitutive Parameter Identification in Plane-Stress Elasto-plastic Problems Using Surface Measurements of Deformation Fields

S. Avril · F. Pierron · Y. Pannier · R. Rotinat

Received: 19 March 2007 / Accepted: 6 August 2007 / Published online: 15 September 2007

Abstract This paper deals with the identification of elasto-plastic constitutive parameters from deformation fields measured over the surface of thin flat specimens with the grid method. The approach for recovering the constitutive parameters is the virtual fields method. A dedicated algorithm is used for deriving the distribution of the 2D stress components from the measured deformation fields. A state of plane stress is assumed. Guesses of the constitutive parameters are input in the algorithm and updated until the stresses satisfy the principle of virtual work in the least squares sense. The advantage of this approach is that it can handle very heterogeneous plastic flows and it is much faster than classical finite element model updating approaches. An experimental application is provided to demonstrate it. Six mild steel double-notched specimens have been tested in a configuration combining tension and in-plane bending. The identified parameters are in good agreement with their reference counterparts. Stress fields are eventually reconstructed across the specimen all along the test for analyzing the evolution of the plastic flow.

Keywords Virtual fields method · Inverse method · Plasticity · Stress localization · Full-field measurements

S. Avril (✉, SEM member) · F. Pierron (SEM member) · Y. Pannier · R. Rotinat (SEM member)
Laboratoire de Mécanique et Procédés de Fabrication,
Ecole Nationale Supérieure d'Arts et Métiers,
Rue Saint-Dominique, BP 508, 51006,
Châlons-en-Champagne Cedex, France
e-mail: stephane.avril@chalons.ensam.fr

Introduction

The identification of elasto-plastic constitutive equations is usually performed on simple test specimens and load configurations, leading to uniform distribution of stresses (tension on a rectangular or cylindrical bar, torsion on a thin tube etc . . .), associated to local strain measurements (extensometers, dial gages or LVDTs, strain gages etc . . .). More sophisticated tests, still using the same measurement techniques, were developed for retrieving more parameters from one test. For instance, using bending tests, it is possible to identify the material behavior in tension and compression, provided that appropriate inverse procedures are developed for processing the local strain measurements [1–4].

The development of optical full-field strain measurements opens the way to novel methodologies based on even more complex tests giving rise to heterogeneous stress and strain fields. Nevertheless, the processing of the data has to resort to some sort of inverse identification since the stress field is not known *a priori*. Finite element model updating is one of the tools that can be used to solve this type of problem [5–12] and most of the time, the experimental implementations presented are based on the use of digital image correlation [6–8, 10, 11]. The idea is to build up a finite element model of the test to be performed using initial input values for the parameters to be retrieved. Then, the experimental data (displacements, strains and/or forces) are compared to the computed ones through a cost function to be minimized. Obviously, issues concerning existence and uniqueness of the solution are of primary importance here and depend greatly on the choice of the test, the amount of measured data and the quality

of the cost function, as discussed for instance by [13]. Computation time is also a critical issue.

The present study is devoted to an alternative technique called the virtual fields method (VFM) [14–16]. The main assets are that several parameters can be obtained simultaneously from one single test, that the VFM is insensitive to parasitic boundary effects which usually disturb the stress fields and that the VFM does not require to elaborate a finite element model for matching measured strain fields. The latter is essential because estimating a few parameters from experimental data can easily take more than 20 h with a finite element model updating approach [11] whereas the VFM can solve the same problem within a few minutes.

In a previous study, an experimental validation of the use of the VFM to identify the parameters of elasto-plastic constitutive equations was presented [16]. A tensile test was carried out on a plane dog-bone specimen. Although not statically determined, this test provided very simple stress and strain distributions because in first approximation, the longitudinal stress only varied as a function of the longitudinal axis of the specimen and the other stress components remained small. The curve of the identified model was in very good agreement with the ones obtained on standard tests using rosettes data [16].

However, in this previous study, only one stress component of the stress tensor was considered and the loading was nearly proportional, thanks to the simple shape of the specimen. In more complex geometries, all the in–plane components of the stress tensor contribute to the principle of virtual work (which is the core of the VFM) and they do not always evolve proportionally. Specifically dedicated algorithms exist in the literature for computing stresses from the experimentally measured in-plane strain fields of a thin plate [14, 17]. The one in [17] is based on the theory of radial return [18] and is faster than the one in [14]. Its implementation in the VFM procedure is presented in this paper, leading up to an *integrated approach* that provides, in a few minutes, the elasto-plastic parameters of a material, without resorting to finite element model updating and whatever the geometry of the specimen (provided that it is flat and thin). This *integrated approach* is validated onto experimental data obtained on a double–notched specimen tested in a configuration combining tension and in-plane bending. After a description of the experimental set-up, of the full-field optical measurement technique and of the identification procedure, results are reported and compared with the ones obtained with standard tests.

Identification Procedure

General Principle

The virtual fields method (VFM) is based on the equilibrium equations which are written in their weak form, called the *principle of virtual work*. This principle can be written as follows for a given solid of volume V subjected to a quasi static loading in absence of body forces:

$$-\int_V \underline{\underline{\sigma}} : \underline{\underline{\varepsilon}}^\star dV + \int_{S_f} T.u^\star dS = 0 \tag{1}$$

where $\underline{\underline{\sigma}}$ is the actual stress tensor, $\underline{\underline{\varepsilon}}^\star$ is the virtual strain tensor, T is the vector of loading tractions acting on the boundary, S_f is the part of the solid boundary where the tractions are applied and $u^\star$ is the virtual displacement field vector. A virtual displacement field is actually a test function, defined across volume V, for which the previous equation is verified, and the virtual strain tensor is the strain tensor derived from the given virtual displacement. An important feature is the fact that $u^\star$ must be kinematically admissible. It means that $u^\star$ must be continuous across the whole volume and it must be null on the boundary where displacements are prescribed [19, 20]. But this condition is the only one required for fulfilling equation (1).

In this study, a state of plane stress is assumed. It is justified because the considered specimens have a constant thickness, denoted b, which is small compared to the other dimensions. Accordingly, only the in-plane components of the stress and strain tensors will be considered. Hence, tensors $\underline{\underline{\sigma}}$ and $\underline{\underline{\varepsilon}}$ are turned into columns σ and ϵ, defined according to the following convention:

$$\sigma = \begin{Bmatrix} \sigma_{xx} \\ \sigma_{yy} \\ \sigma_{xy} \end{Bmatrix} \quad \text{and} \quad \epsilon = \begin{Bmatrix} \epsilon_{xx} \\ \epsilon_{yy} \\ 2\epsilon_{xy} \end{Bmatrix} \tag{2}$$

Both σ and ϵ are functions of three variables: time t and space variables x and y. Quantity $\epsilon(x, y, t)$ can be computed by differentiating the measured displacement fields, denoted $u(x, y, t)$, with regard to x and y:

$$\epsilon = \begin{Bmatrix} \epsilon_{xx} \\ \epsilon_{yy} \\ 2\epsilon_{xy} \end{Bmatrix} = \begin{Bmatrix} \frac{\partial u_x}{\partial x} \\ \frac{\partial u_y}{\partial y} \\ \frac{\partial u_x}{\partial y} + \frac{\partial u_y}{\partial x} \end{Bmatrix} \tag{3}$$

The infinitesimal formulation of the strain tensor is used in this work because the strains remain lower than 2.5%. However, for a possible further use of the procedure with higher strains, the Green-Lagrange

tensor may be used instead [21], as $u(x, y, t)$ is provided in the initial configuration. Numerical issues concerning the differentiation are discussed in "Numerical Aspects."

For deriving quantity $\sigma(x, y, t)$ in equation (4), the constitutive equations must be introduced. In order to include both elasticity and plasticity in a general framework, the stress rate $\dot{\sigma} = d\sigma/dt$ may be written like this:

$$\dot{\sigma} = g(\dot{\epsilon}, \sigma, X) \tag{4}$$

where g is a given vectorial function of the actual strain rate $\dot{\epsilon} = d\epsilon/dt$, of the actual stress σ and of the unknown constitutive parameters. The latter are denoted X when designated entirely and X_p when designated individually, $1 \leq p \leq P$, where P is the number of unknown constitutive parameters. Equation (4) provides an *implicit* definition of the stresses, as $\dot{\sigma}$ depends on σ. Using this implicit definition, equation (1) may be rewritten as:

$$-b \int_{\mathrm{A}} \left[\int_0^t g(\dot{\epsilon}, \sigma, X) dt \right] . \epsilon^\star dS + \int_{S_f} T.u^\star dS = 0 \tag{5}$$

where A is the measurement area and b is the thickness of the specimen; b has been factorized out of the first integral thanks to the assumption of plane stress.

The quantity $\dot{\epsilon}(x, y, t)$ can be derived from the displacement fields measured all along the deformation of the solid. Therefore, at a given time t and for a given virtual field $u^\star$, only the X parameters are unknown in equation (5). At least as many equations as unknowns are needed to recover them. It is a trivial matter to see that two approaches may provide different equations involving the unknown X parameters:

- Either by writing equation (5) with different virtual fields,
- Or by writing equation (5) at different times during the deformation of the solid with the same virtual field.

Both approaches can be combined. The objective is to build up a system where the equations are sufficiently independent to involve all the unknown parameters. The system may be overdetermined to increase the redundancy and hence to decrease the uncertainty of the results.

Actually, equations derived from equation (5) can be of different nature, depending on g. If g is a linear function of the X_p and does not depend on σ (linear elasticity for instance), the time integration is explicit in equation (5). Thus, linear equations involving the unknown parameters can be easily deduced from equation (5) for a linear elastic behavior [19, 20]. But in the case of plasticity, the time integration cannot be simplified because equation (4) is a first order differential equation of $\sigma(t)$ at each location (x, y). This issue is addressed in the following section.

Definition of the Present Constitutive Equations

Standard characterization of the material

The material studied here is mild steel with less than 0.5% carbon. It is supplied as 2 mm-thick sheets in

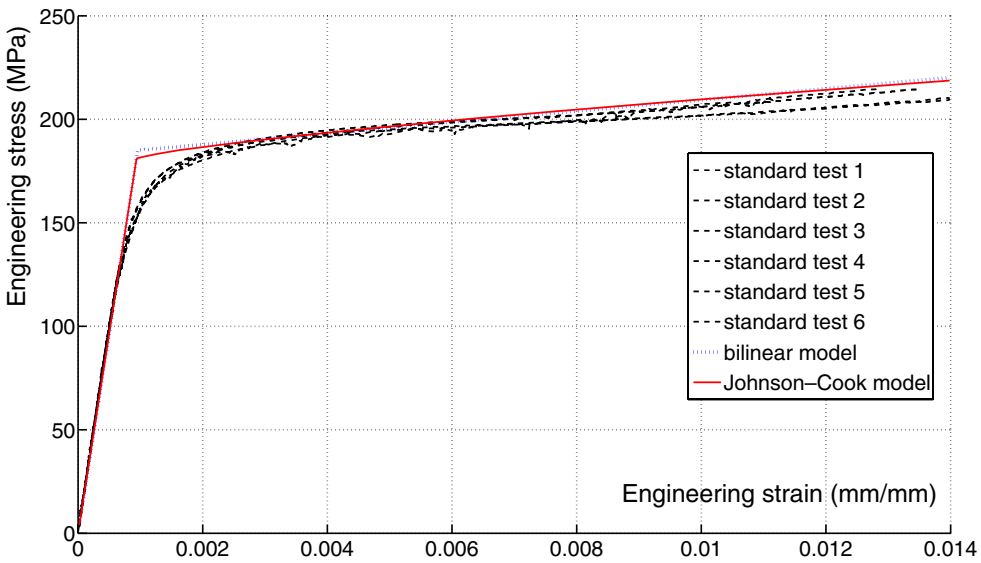

Fig. 1 Response of the material subjected to standard tension and identified models

which the coupons are cut. The material was first characterized by standard tension on prismatic coupons. Five specimens were tested. The obtained stress-strain curves (dotted lines in Fig. 1) showed that the material is linear elastic isotropic before yielding. Its constitutive equations are characterized by Young's modulus denoted E and Poisson's ratio denoted ν. Both constants have been identified during the standard tensile tests using the longitudinal and transverse strain values measured by rosettes. In order to get linear relationships between strains and stresses, the two following parameters (stiffness components) are defined: $X_1 = E/(1-\nu^2)$ and

$$X_2 = \nu E/\left(1-\nu^2\right).$$

For the range of strains $0.003 < \epsilon < 0.014$ (plastic regime), a linear function can be considered for modelling the behavior of the material which is investigated here (Fig. 1). Accordingly, an isotropic linear hardening model may be suited for this material when it is subjected to monotonic loading [18]. Even though kinematic hardening may be combined with isotropic hardening, the effects are not detectable in the monotonic loading response. Therefore, only two other constitutive parameters are introduced for the model: X_3, which is the initial yield stress and X_4, which is the hardening modulus.

Reference values of X_1, X_2, X_3 and X_4 for the material of this study were identified from the standard tensile tests. They are reported in Table 2.

The purpose of this study is to identify the same parameters using a test where the strains and stresses are heterogeneous. To this purpose, function g in equation (4) must be explicitly written in function of X_1, X_2, X_3 and X_4.

Basic equations of time independent plasticity

Several assumptions are made in this study: small perturbations, plane stress, isotropy in elasticity and plasticity, decomposition of total strains in an elastic part and a plastic part: $\epsilon = \epsilon^{\mathrm{el}} + \epsilon^{\mathrm{p}}$, volume conservation in plasticity and time independent plasticity. Time independent plasticity [18] provides the mathematical relationships required to provide explicitly function g defined in equation (4). Time independent plasticity is based on the following concepts:

1. The *yield function* which defines the limits of the linear elastic domain;
2. The *flow rule* which is the function characterizing the evolution of the cumulative equivalent plastic strain, denoted p, defined as:

$$p = \int_0^t \dot{p}dt = \int_0^t \sqrt{\frac{2}{3}\left[(\dot{\epsilon}^{\mathrm{p}}_{xx})^2 + (\dot{\epsilon}^{\mathrm{p}}_{yy})^2 + (\dot{\epsilon}^{\mathrm{p}}_{zz})^2 + 2(\dot{\epsilon}^{\mathrm{p}}_{xy})^2\right]}dt \tag{6}$$

3. The *hardening law* which gives the evolution of the limits of the linear elastic domain in function of p.

As volume is conserved, the yield function depends on the deviatoric stress but not on the hydrostatic stress. This is assumed here, where the deviatoric stress $\underline{\underline{s}}$ is defined like this:

$$\underline{\underline{s}} = \begin{Bmatrix} s_{xx} & s_{xy} & 0 \\ s_{xy} & s_{yy} & 0 \\ 0 & 0 & -(s_{xx}+s_{yy}) \end{Bmatrix} \quad \text{with}$$

$$\begin{Bmatrix} s_{xx} \\ s_{yy} \\ s_{xy} \end{Bmatrix} = \begin{Bmatrix} 2\sigma_{xx}/3 - \sigma_{yy}/3 \\ 2\sigma_{yy}/3 - \sigma_{xx}/3 \\ \sigma_{xy} \end{Bmatrix} \tag{7}$$

Different yield functions exist in isotropic plasticity. The most simple one, which is used here, is based on the Von Mises equivalent stress, denoted σ_{eq}, which is defined as:

$$\sigma_{\mathrm{eq}} = \sqrt{\sigma_{xx}^2 + \sigma_{yy}^2 - \sigma_{xx}\sigma_{yy} + 3\sigma_{xy}^2} \tag{8}$$

Therefore, the Von Mises yield function may be written as:

$$f(\sigma, p) = \sigma_{\mathrm{eq}}^2 - \sigma_s(p)^2 = \sigma_{xx}^2 + \sigma_{yy}^2 - \sigma_{xx}\sigma_{yy} + 3\sigma_{xy}^2 - \sigma_s(p)^2 = 0 \tag{9}$$

The σ_s stress is the yield stress at the current state. It is larger than the initial yield stress, denoted σ_0 (the X_3 parameter defined in this study) because of hardening. It may depend on different variables but only an isotropic hardening model with a dependence on p is considered in this study because the loading path is monotonic.

A plastic flow occurs when two conditions are satisfied simultaneously:

1. The stresses are already on the yield surface, meaning that the yield function is null:

$$f(\sigma, p) = 0 \tag{10}$$

2. The stresses remain on the yield surface, meaning that the yield function remains null:

$$df = \frac{\partial f}{\partial \sigma} : d\sigma + \frac{\partial f}{\partial p} dp = 0 \tag{11}$$

From the latter equation results Hill's principle stating that the plastic strain vector should be perpendicular to the yield surface. The following flow rule can be deduced:

$$\dot{\epsilon^p} = \dot{\lambda} \frac{\partial f}{\partial \sigma} \tag{12}$$

where $\dot{\lambda}$ is the plastic flow factor.

It can be deduced from equation (9) that:

$$\frac{\partial f}{\partial \sigma} = s \tag{13}$$

So:

$$\dot{\epsilon^p} = \dot{\lambda} s = \frac{3}{2} \frac{s}{\sigma_s} \dot{p} \tag{14}$$

It can also be deduced from equation (9) that:

$$\frac{\partial f}{\partial p} = -\frac{2}{3} \frac{\partial \sigma_s}{\partial p}(p) \sigma_s(p) \tag{15}$$

Therefore, turning dp into $\dot{p}$ and $d\sigma$ into $\dot{\sigma}$, equation (11) becomes:

$$s : \dot{\sigma} - \frac{4}{9} \frac{\partial \sigma_s}{\partial p}(p) [\sigma_s(p)]^2 \dot{\lambda} = 0 \tag{16}$$

If the linear model is considered: $\sigma_s(p) = \sigma_0 + Hp$, where H is the X_4 parameter defined in this study, then, $\partial \sigma_s / \partial p(p) = H = X_4$.

Decomposing the total strain in its elastic and plastic parts and introducing Hooke's law in plane stress, one gets:

$$\begin{aligned}
\dot{\sigma} &= \begin{bmatrix} X_1 & X_2 & 0 \\ X_2 & X_1 & 0 \\ 0 & 0 & X_1 - X_2 \end{bmatrix} \begin{Bmatrix} \dot{\epsilon}^{\mathrm{el}}_{xx} \\ \dot{\epsilon}^{\mathrm{el}}_{yy} \\ \dot{\epsilon}^{\mathrm{el}}_{xy} \end{Bmatrix} \\
&= \begin{bmatrix} X_1 & X_2 & 0 \\ X_2 & X_1 & 0 \\ 0 & 0 & X_1 - X_2 \end{bmatrix} \begin{Bmatrix} \dot{\epsilon}_{xx} - \dot{\epsilon}^{\mathrm{p}}_{xx} \\ \dot{\epsilon}_{yy} - \dot{\epsilon}^{\mathrm{p}}_{yy} \\ \dot{\epsilon}_{xy} - \dot{\epsilon}^{\mathrm{p}}_{xy} \end{Bmatrix} \\
&= \begin{bmatrix} X_1 & X_2 & 0 \\ X_2 & X_1 & 0 \\ 0 & 0 & X_1 - X_2 \end{bmatrix} \begin{Bmatrix} \dot{\epsilon}_{xx} - \dot{\lambda} s_{xx} \\ \dot{\epsilon}_{yy} - \dot{\lambda} s_{yy} \\ \dot{\epsilon}_{xy} - \dot{\lambda} s_{xy} \end{Bmatrix}
\end{aligned} \tag{17}$$

Combining equations (16) and (17) provides an equation with only $\dot{\lambda}$ as unknown. The resolution yields:

$$\dot{\lambda} = \frac{(X_1 \dot{\epsilon}_{xx} + X_2 \dot{\epsilon}_{yy}) s_{xx} + (X_1 \dot{\epsilon}_{yy} + X_2 \dot{\epsilon}_{xx}) s_{yy} + 2(X_1 - X_2) \dot{\epsilon}_{xy} s_{xy}}{(X_1 s_{xx} + X_2 s_{yy}) s_{xx} + (X_1 s_{yy} + X_2 s_{xx}) s_{yy} + 2(X_1 - X_2) s_{xy} s_{xy} + \frac{4}{9} X_4 \sigma_s^2} \tag{18}$$

Equations (17) and (18) are satisfied only when the behavior is plastic. This implies that $\dot{\lambda}$ must be positive.

Derivation of the constitutive equations

Function g defined in equation (4) can be derived from equations (17) and (18):

$$\begin{aligned}
g(\dot{\epsilon}, \sigma, X) &= \begin{Bmatrix} g_1(\dot{\epsilon}, \sigma, X) \\ g_2(\dot{\epsilon}, \sigma, X) \\ g_6(\dot{\epsilon}, \sigma, X) \end{Bmatrix} \\
&= \begin{bmatrix} X_1 & X_2 & 0 \\ X_2 & X_1 & 0 \\ 0 & 0 & X_1 - X_2 \end{bmatrix} \begin{Bmatrix} \dot{\epsilon}_{xx} - \langle \dot{\lambda} \rangle s_{xx} \\ \dot{\epsilon}_{yy} - \langle \dot{\lambda} \rangle s_{yy} \\ \dot{\epsilon}_{xy} - \langle \dot{\lambda} \rangle s_{xy} \end{Bmatrix}
\end{aligned} \tag{19}$$

where $\langle x \rangle$ means that $\langle x \rangle = x$ if $x > 0$ and $\langle x \rangle = 0$ otherwise; $\dot{\lambda}$ is defined such as:

$$\text{if} \quad f(\sigma, p) < 0, \quad \dot{\lambda} = 0$$

$$\text{if} \quad f(\sigma, p) = 0,$$

$$\dot{\lambda} = \frac{(X_1 \dot{\epsilon}_{xx} + X_2 \dot{\epsilon}_{yy}) s_{xx} + (X_1 \dot{\epsilon}_{yy} + X_2 \dot{\epsilon}_{xx}) s_{yy} + 2(X_1 - X_2) \dot{\epsilon}_{xy} s_{xy}}{(X_1 s_{xx} + X_2 s_{yy}) s_{xx} + (X_1 s_{yy} + X_2 s_{xx}) s_{yy} + 2(X_1 - X_2) s_{xy} s_{xy} + \frac{4}{9} X_4 \sigma_s^2} \tag{20}$$

This definition of function g handles both elastic and plastic behaviors. Indeed, it can be noticed that $\langle \dot{\lambda} \rangle$ used in equation (19) represents the plastic flow factor only if the behavior is plastic. Otherwise, the behavior is elastic and $\langle \dot{\lambda} \rangle$ is zero. This occurs by two different ways:

1. The behavior was previously plastic and becomes purely elastic due to unloading. This is the reason why the notation $\langle x \rangle$ is used;
2. The behavior was previously elastic and remains elastic. This is the reason why $\dot{\lambda} = 0$ is prescribed when $\sigma_s < X_3$ in equation (20).

Identification Scheme

The specimen used in this study for providing a heterogeneous strain distribution is shown in Fig. 2. Measurements of the displacement fields are available in the

area of interest shown in the figure. The measurements are performed at different times evenly distributed all along the test, before and after the onset of plasticity. These times are denoted t_i and the tensile resultant load, denoted F_i, is also measured at these given times. The number of measurement times is denoted m. It lies between 60 and 70 in the present experiments.

Strains and stresses in the measurement area are heterogeneous. Their gradients can be quite large at the notch tip. The purpose here is to use the measured displacements for deriving a system of equations from equations (5), (19) and (20), and to solve it for identifying X_1, X_2, X_3 and X_4.

Equations are derived firstly by writing equation (5) at different times with the following virtual field:

$$\begin{cases} u_x^\star = 0 \\ u_y^\star = y \end{cases} \Rightarrow \begin{cases} \epsilon_{xx}^\star = 0 \\ \epsilon_{yy}^\star = 1 \\ \epsilon_{xy}^\star = 0 \end{cases} \tag{21}$$

Accordingly, up to m equations can be derived, which may be written:

$$\frac{1}{\mathrm{A}} \int_{\mathrm{A}} \left[\int_0^{t_i} g_2(\dot{\epsilon}, \sigma, X) dt \right] dS = \frac{F_i L}{b\,\mathrm{A}} \tag{22}$$

where L is the length of the area of interest (Fig. 2).

The separation of the X_1 and X_2 contributions from the previous equations is actually not possible because Poisson's effect during the elastic behavior is filtered out with the virtual field written in equation (21). Indeed, this virtual field only involves the longitudinal stress but not the other components. Other equations are required. Therefore, a second virtual field is considered, denoted $u^{\star\nu}$. It is defined with a basis of piecewise linear functions. This virtual field cancels out the contribution of the resultant load F_i in equation (5) and it is chosen so as to maximize the identifiability of Poisson's ratio, according to the theory detailed in [22]. The effect of $u^{\star\nu}$ over the measurement area is shown in Fig. 3(b). It has a lateral shrinking effect. Introducing this second virtual field in equation (5), one gets other equations, which may be written as:

$$\int_{\mathrm{A}} \left[\int_0^{t_i} g(\dot{\epsilon}, \sigma, X) dt \right] . \epsilon^{\star\nu} dS = 0 \tag{23}$$

Equations (22) and (23) provide a system of equations involving the unknown parameters X_1, X_2, X_3 and X_4. No more virtual fields are required here. Actually, the use of more complicated virtual fields has not been tested as it will be shown that the ones presented in equation (21) and in Fig. 3(b) provide very good results. It is worth noting that, except for Poisson's ratio, all the information needed for identifying the constitutive parameters is contained here in stress component σ_{yy}. The choice of relevant virtual fields may become a critical issue when dealing with anisotropic elasto-plasticity as one would have to filter out the contribution of a larger number of parameters into the global response of the specimen. A study is currently underway for solving this issue, based on the same principles as the one presented in [23].

The system of equations that one has to solve here is overdetermined as up to $2m$ equations may be derived from equations (22) and (23). It will be shown further ("Identification Results") that less equations may be used to speed up the resolution. However, for the sake of simplicity, let us consider that equations (22) and (23) are written each time measurements are available. The obtained system of $2m$ equations is solved in

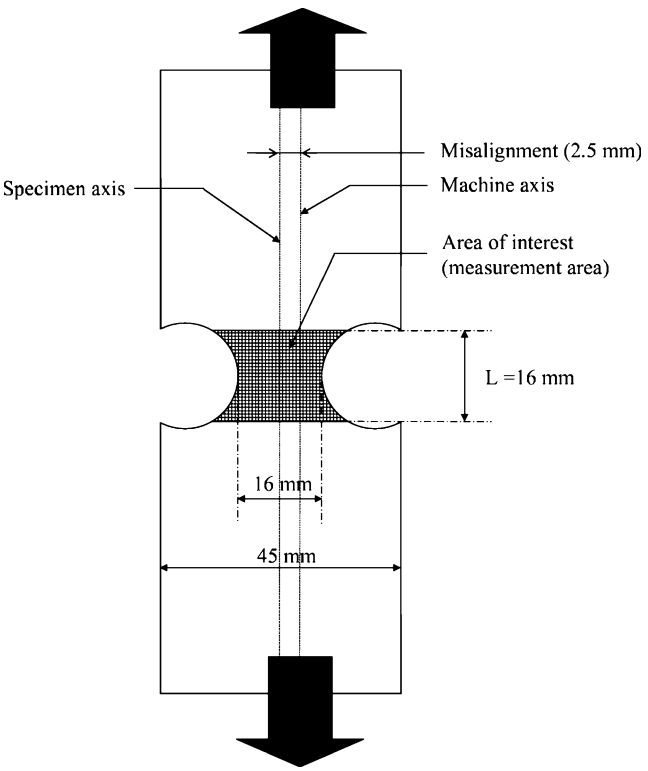

Fig. 2 Sketch of the double-notched specimen

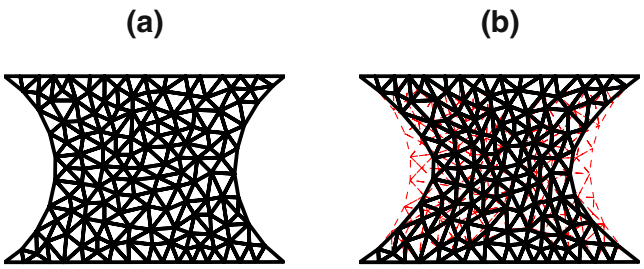

Fig. 3 (**a**) Mesh used in the measurement area (undeformed). (**b**) Virtual mesh deformation for identifying Poisson's ratio

the least squares sense, which means that X_1, X_2, X_3 and X_4 are searched as the minimum of the following cost function:

$$\mathcal{F}(X) = \sum_{i=1}^{m}\left[\int_0^{t_i}\frac{1}{\mathrm{A}}\int_{\mathrm{A}} g_2(\dot{\epsilon},\sigma,X)dSdt - \frac{F_i L}{b\,\mathrm{A}}\right]^2 + \sum_{i=1}^{m}\left[\int_0^{t_i}\int_{\mathrm{A}} g(\dot{\epsilon},\sigma,X).\epsilon^{\star v}dSdt\right]^2 \quad (24)$$

Numerical Aspects

A numerical approach has been implemented for computing the integrals in equation (24). It is based on two stages:

1. The strain fields are reconstructed from the measurements using a basis of functions similar to the one used in the Finite Elements Method,
2. The stress fields are reconstructed by computing approximated values of g according to equations (19) and (20).

Numerical aspects related to these two stages and to the minimization of the cost function are discussed in this section.

Reconstruction of strain fields

For filtering purposes, the displacement fields measured in the area of interest (Fig. 2) are projected onto a basis of piecewise linear functions, denoted φ_k. This provides a "finite element" reconstruction of the displacement field, computed directly from the measurements [24], i.e. nodal values are derived directly from the experimental data, without solving any forward problem.

The piecewise linear functions are actually the same basis functions which are used to define $u^{\star v}$. The measurement area is meshed using triangles [Fig. 3(a)]. The number of triangles is denoted N and the number of nodes K. Each function φ_k equals 1 at a given node0000 of the mesh and 0 at all the other nodes. The reconstructed displacement fields can be written:

$$\begin{cases} u_x(x,y,t) = \sum_{k=1}^{K} a_k(t)\varphi_k(x,y) \\ u_y(x,y,t) = \sum_{k=1}^{K} b_k(t)\varphi_k(x,y) \end{cases} \quad (25)$$

where $a_k(t)$ and $b_k(t)$ are obtained by regression in the least squares sense each time measurements are available. Then, the displacement fields reconstructed with the basis functions are used to deduce the strain fields required for the identification.

$$\epsilon(x,y,t) = \begin{Bmatrix} \epsilon_{xx}(x,y,t) \\ \epsilon_{yy}(x,y,t) \\ 2\epsilon_{xy}(x,y,t) \end{Bmatrix} = \begin{Bmatrix} \sum_{k=1}^{K} a_k(t)\frac{\partial\varphi_k(x,y)}{\partial x} \\ \sum_{k=1}^{K} b_k(t)\frac{\partial\varphi_k(x,y)}{\partial y} \\ \sum_{k=1}^{K} a_k(t)\frac{\partial\varphi_k(x,y)}{\partial y} + \sum_{k=1}^{K} b_k(t)\frac{\partial\varphi_k(x,y)}{\partial x} \end{Bmatrix} \quad (26)$$

Differentiating the φ_k basis functions provides strain fields which are constant in each triangle (Fig. 6).

Reconstruction of stress fields

Let (x_n, y_n) denote the center of gravity and A_n the area of each triangle. The value of g for a given triangle T_n at a given time t is approximated according to equations (19) and (20). A large number of measurements are achieved all along the tests, with a constant time increment denoted τ. Therefore, for computing the stress value for a given triangle T_n at a given time t_{i+1}, one must compute before the stress value for the given triangle T_n at all the previous time steps.

A recursive algorithm is used, based on the one published in [17]. In this recursive algorithm, the stress rate and the strain rate are assumed constant between two consecutive measurement steps. This assumption is justified because the strain increment between two consecutive measurements remains lower than 5.10^{-4}.

The stresses must be known at time t_1 to initiate the recursive algorithm. Time t_1 is chosen as the time when the specimen is unloaded, so as to ensure $\sigma(x_n, y_n, t_1) = 0$. Then, at each time t_i, $\sigma(x_n, y_n, t_{i+1})$ is deduced from $\sigma(x_n, y_n, t_i)$ in two stages. At the first stage, an estimate is provided according to:

$$\tilde{\sigma}(x_n,y_n,t_{i+1}) = \sigma(x_n,y_n,t_i) + \tau\, g\left(\frac{\epsilon(x_n,y_n,t_{i+1}) - \epsilon(x_n,y_n,t_i)}{\tau}, \sigma(x_n,y_n,t_i), X\right) \quad (27)$$

However, this estimate may be inaccurate because of the linearization of stress and strain variations between t_{i+1} and t_i. Thus $\sigma(x_n, y_n, t_{i+1})$ may be different of $\tilde{\sigma}(x_n, y_n, t_{i+1})$ in practice.

Therefore, a second stage is required for the correction. Four cases must be distinguished, depending on the values of the Von Mises yield function $f(\sigma, p)$ defined in equation (9):

1. If $f(\sigma(x_n, y_n, t_{i+1}), p(t_i)) < 0$ and $f(\tilde{\sigma}(x_n, y_n, t_{i+1}), p(t_i)) < 0$, the behavior is elastic at t_i and remains elastic at t_{i+1}. Then, no correction is required and $\sigma(x_n, y_n, t_{i+1}) = \tilde{\sigma}(x_n, y_n, t_{i+1})$
2. If $f(\sigma(x_n, y_n, t_{i+1}), p(t_i)) = 0$ and $f(\tilde{\sigma}(x_n, y_n, t_{i+1}), p(t_i)) < 0$, the behavior is plastic at t_i and becomes elastic at t_{i+1}. Then, no correction is required and $\sigma(x_n, y_n, t_{i+1}) = \tilde{\sigma}(x_n, y_n, t_{i+1})$
3. If $f(\sigma(x_n, y_n, t_{i+1}), p(t_i)) = 0$ and $f(\tilde{\sigma}(x_n, y_n, t_{i+1}), p(t_i)) \geq 0$, the behavior is plastic at t_i and remains plastic at t_{i+1}. There is an increment of plastic strain that can be assessed according to:

$$\begin{Bmatrix} \Delta\epsilon^{\mathrm{p}}_{xx}(t_i) \\ \Delta\epsilon^{\mathrm{p}}_{yy}(t_i) \\ \Delta\epsilon^{\mathrm{p}}_{xy}(t_i) \end{Bmatrix} = \frac{1}{\tau} \begin{Bmatrix} \epsilon_{xx}(t_{i+1}) - \epsilon_{xx}(t_i) \\ \epsilon_{yy}(t_{i+1}) - \epsilon_{yy}(t_i) \\ \epsilon_{xy}(t_{i+1}) - \epsilon_{xy}(t_i) \end{Bmatrix} - \frac{1}{\tau} \begin{bmatrix} X_1 & X_2 & 0 \\ X_2 & X_1 & 0 \\ 0 & 0 & X_1 - X_2 \end{bmatrix}^{-1} \times \begin{Bmatrix} \tilde{\sigma}_{xx}(t_{i+1}) - \sigma_{xx}(t_i) \\ \tilde{\sigma}_{yy}(t_{i+1}) - \sigma_{yy}(t_i) \\ \tilde{\sigma}_{xy}(t_{i+1}) - \sigma_{xy}(t_i) \end{Bmatrix} \tag{28}$$

The equivalent plastic strain at time t_{i+1} can be approximated by:

$$p(t_{i+1}) = p(t_i) + \sqrt{\frac{2}{3}\left[(\Delta\epsilon^{\mathrm{p}}_{xx}(t_i))^2 + (\Delta\epsilon^{\mathrm{p}}_{yy}(t_i))^2 + \left(\frac{\Delta\epsilon^{\mathrm{p}}_{xx}(t_i) + \Delta\epsilon^{\mathrm{p}}_{yy}(t_i)}{2}\right)^2 + 2(\Delta\epsilon^{\mathrm{p}}_{xy}(t_i))^2\right]} \tag{29}$$

The value of $f(\tilde{\sigma}(x_n, y_n, t_{i+1}), p(t_{i+1}))$ should be zero but a slight mismatch may occur due to the linearization of the stress variations between t_i and t_{i+1}. This means that a correction of $\tilde{\sigma}(x_n, y_n, t_{i+1})$ is needed for approximating the actual stress $\sigma(x_n, y_n, t_{i+1})$. This is addressed by radial return. One prescribes: $\sigma(x_n, y_n, t_{i+1}) = [1-\beta]\tilde{\sigma}(x_n, y_n, t_{i+1})$, where β is computed such as:

$$f([1-\beta]\tilde{\sigma}(x_n, y_n, t_{i+1}), p(t_{i+1})) = 0 \tag{30}$$

The reconstructed stress at time t_{i+1} is eventually: $\sigma(x_n, y_n, t_{i+1}) = [1-\beta]\tilde{\sigma}(x_n, y_n, t_{i+1})$. It has been verified using simulated data that the remaining error using this correction is lower than 0.1% of the actual stress when the strain increments between two consecutive time steps are lower than 5.10^{-4}.

4. if $f(\sigma(x_n, y_n, t_{i+1}), p(t_i)) < 0$ and $f(\tilde{\sigma}(x_n, y_n, t_{i+1}), p(t_i)) \geq 0$, the behavior is elastic at t_i and becomes plastic between t_i and t_{i+1}. The time of the transition between elasticity and plasticity is approximated by:

$$t_T = t_i + \alpha\tau \tag{31}$$

with α computed such as:

$$f(\alpha\tilde{\sigma}(x_n, y_n, t_{i+1}), p(t_i))) = 0 \tag{32}$$

Then a new stress value, $\hat{\sigma}$ is assessed at time t_{i+1}:

$$\hat{\sigma}(x_n, y_n, t_{i+1}) = \sigma(x_n, y_n, t_i) + (1-\alpha) \times \tau\, g\left(\frac{\epsilon(x_n, y_n, t_{i+1}) - \epsilon(x_n, y_n, t_i)}{\tau}, \alpha\tilde{\sigma}(x_n, y_n, t_i), X\right) \tag{33}$$

Eventually, $\sigma(x_n, y_n, t_{i+1})$ is deduced from $\hat{\sigma}(x_n, y_n, t_{i+1})$ according to the procedure described at point 3.

Sutton et al. [17] mentioned a fifth case, which is actually a numerical artifact, and where $f(\sigma(x_n, y_n, t_{i+1}), p(t_i)) = 0$ and $\dot{\lambda} < 0$ [$\dot{\lambda}$ defined in equation (18)] but $f(\tilde{\sigma}(x_n, y_n, t_{i+1}), p(t_i)) \geq 0$. It was called the "negative plastic flow" by the authors and only occurs when the strain increment between two consecutive times is locally very large. If a "negative plastic flow" is detected, the strain increment is split in sub-increments for removing this effect. No "negative plastic flow" was detected in processing the experiments shown further in this study.

Identification of constitutive parameters

The following functions have a constant value in any triangle according to the reconstruction scheme: $\epsilon^{\star\nu}$, $\dot{\epsilon}$ and σ. Therefore, equation (24) may be written as:

$$\mathcal{F}(X) = \sum_{i=1}^{m}\left[\sum_{n=1}^{N}\left(\frac{\mathrm{A}_n}{\mathrm{A}}\int_0^{t_i} g_2(\dot{\epsilon}(x_n, y_n, t), \sigma(x_n, y_n, t), X)\, dt\right) - \frac{P_i L}{b\,\mathrm{A}}\right]^2 + \sum_{i=1}^{m}\left[\sum_{n=1}^{N}\mathrm{A}_n\left(\int_0^{t_i} g(\dot{\epsilon}(x_n, y_n, t), \sigma(x_n, y_n, t), X)\, dt\right) . \epsilon^{\star\nu}(x_n, y_n)\right]^2 \tag{34}$$

The time integration of g between 0 and t_i required in equation (34) is achieved according to the scheme

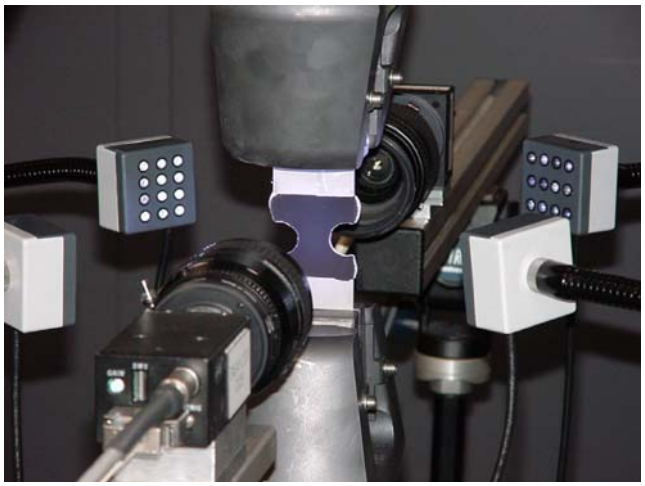

Fig. 4 Picture of the mechanical and optical set-up

discussed in "Reconstruction of stress fields." It is interesting to note that this time integration can be achieved for any given constitutive parameters X. Eventually, the identified constitutive parameters are the ones that minimize $\mathcal{F}(X)$ and the stresses reconstructed with these identified parameters according to the scheme described in "Reconstruction of stress fields" are the ones that fit at best the actual stresses.

The minimum of $\mathcal{F}(X)$ is found with the Nelder–Mead approach in 50 iterations (about 1 min with a Pentium M processor, 1,400 MHz). Existence and uniqueness of the minimum are investigated by trial and error directly onto the experimental data.

A minimization algorithm based on the gradients of the cost function is under development. It may speed up the convergence when constitutive equations with a large number of parameters are considered. However, computation time was not a critical issue here as only 4 parameters were unknown and it will be shown in Section Identification Results that only two are actually searched by the minimization approach. Moreover, it is worth pointing out that no finite element computation are performed here at any stage. Therefore, minimization is very fast compared to finite element model updating approaches that require to solve a large number of forward problems for identifying the same number of constitutive parameters. Even in its current state (Nelder–Mead approach), the computation time of the VFM is at least 100 times less than the computation time of finite element updating approaches (20 h mentioned in [11]).

Application to Experimental Data

The approach presented in this paper for characterizing the elasto-plastic properties of metals can be applied to any geometry of flat specimen, as long as the assumption of plane stress is satisfied (this aspect was discussed in [14]). Moreover, there is no need to make assumptions about the boundary conditions, only the load resultant has to be measured. These aspects represent important assets because the specimen shape and the boundary conditions can be chosen without any constraint for characterizing the material behavior. An example of application is shown in this section for highlighting these assets.

Optical and Mechanical Set-up

Six specimens having the shape shown in Fig. 2 were tested. They were loaded in tension up to 8 kN at a cross-head rate of 0.05 mm/min. A picture of one of these specimens, along with the mechanical and optical arrangements (grips, lights, cameras) is shown in Fig. 4. The specimens are not subjected to pure tension. The axis of the specimen is slightly misaligned with regard to the axis of the tensile load. The distance between both axes is 2.5 mm (Fig. 2). Accordingly, applying a tensile load will result also in an in-plane moment, inducing in-plane bending along with the main tensile response of the double-notched specimen. The purpose of using this misalignment is just to demonstrate that pure tension is not required for using the present identification approach, because it can handle any type of boundary conditions provided that the resultant load is measured. Moreover, it will be shown further that using this misalignment enriches the test with interesting yield flow directions.

About 60 images were recorded all along the test ($\tau = 30$ s). In-plane displacement fields were measured across the area of interest shown in Fig. 2 from these images.

The optical technique used here for measuring in-plane displacement fields in the area of interest is the grid method [16]. It is a non interferometric white light technique aimed at measuring 2D displacement fields. A contrasted network of cross-lines (the grid) is transferred onto the area of interest [25]. This network of contrasted lines acts as a visual encoding of the surface of the tested specimen. A digital camera performs the spatial sampling and acquisition of the intensity of the grid. It can be shown that the deformation of the grid between the deformed and undeformed states leads to a phase modulation of the sampled intensity signal. An algorithm based on spatial phase stepping [26] enables the measurement of the phase maps. Another algorithm enables the separation of the information from both directions x and y by averaging the signal in the other direction over two periods.

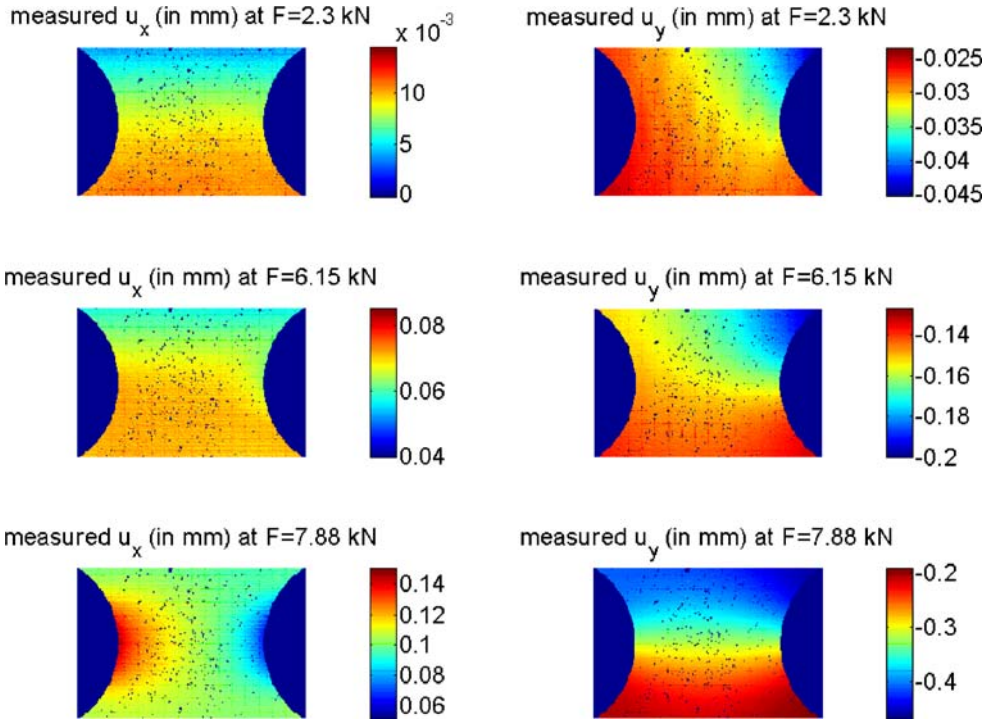

Fig. 5 Displacement fields measured at different times

Nevertheless, because of the use of an imaging lens, the measurements of the in-plane displacements are sensitive to out-of-plane movements of the specimen. Indeed, the magnification depends on the imaging distance and any change of this distance will induce a change of magnification that the system will interpret as strains. A simple model of thin lens gives a linear relationship between the out-of-plane movement and the induced "strains." During the tests, out-of-plane movements up to 0.15 mm gave rise to parasitic strains up to 1.10^{-3}, which was not compatible with the requirements of the experiments. The use of a telecentric

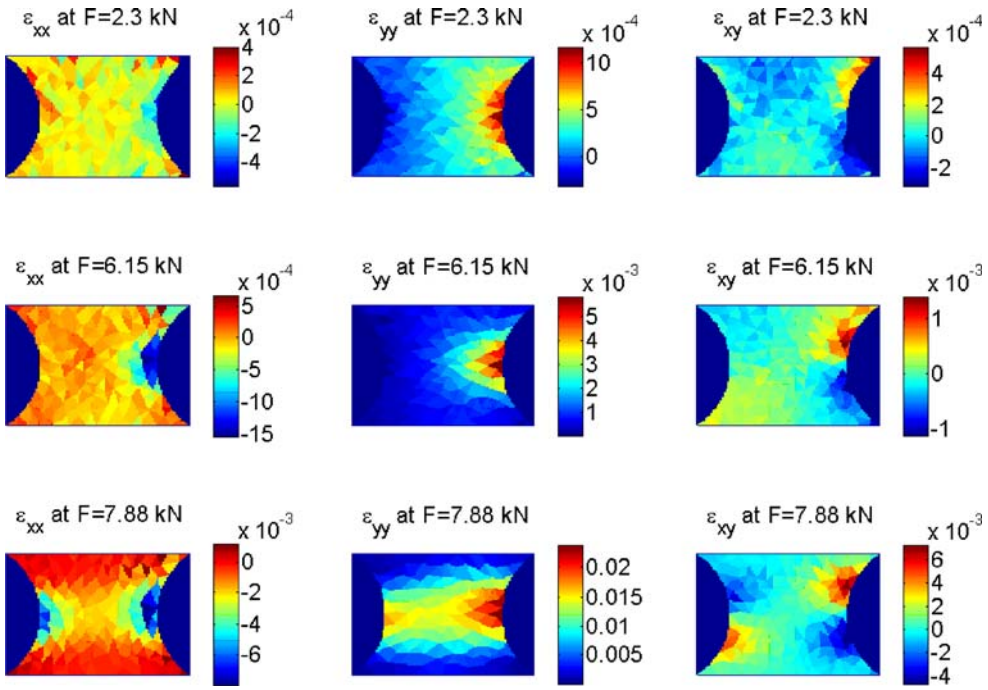

Fig. 6 Discontinuous strain fields derived from the reconstructed piecewise linear displacement fields at different times

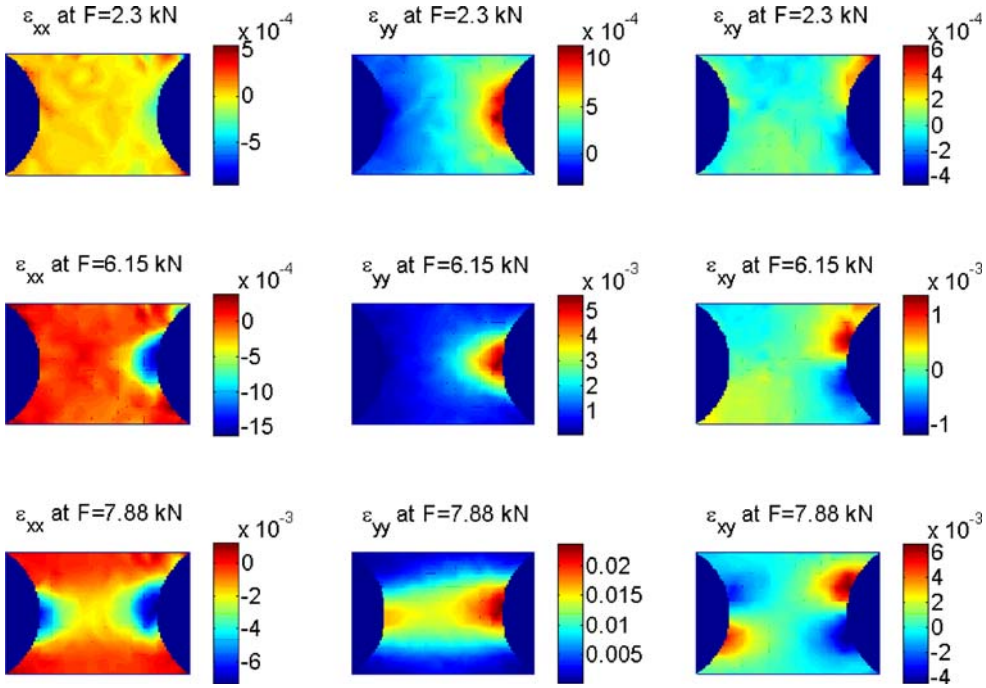

Fig. 7 Continuous strain fields reconstructed from the measurements at different times

lens would solve that problem but other issues like lighting, cost and lack of flexibility makes this solution rather inconvenient. Another possibility to get rid of this problem consists in measuring the displacements on both sides of the specimen using two cameras. Indeed, if the cameras are positioned symmetrically with respect to the specimen plane (Fig. 4), the effects of the out-of-plane movements cancel out when averaging the phase maps from both CCD cameras. This procedure has also the advantage of cancelling possible parasitic out-of-plane bending strains caused by some misalignment and clearance of the grips, in the same spirit as the procedure with back-to-back strain gages used for the reference tests.

Analysis of Strain Fields

The measured displacement fields cannot be differentiated using local differentiation by the finite difference method. The resolution of the measurements was about 1 μm. Even if this performance is interesting (see raw data in Fig. 5), direct differentiation is highly sensitive to the noise and the resolution of the derived strains could not be brought down below 10^{-3}, which is insufficient here. In order to address this issue, the measured displacement fields are fitted using a basis of piecewise linear functions, as explained before. The mesh shown in Fig. 3 is used. The average mesh size is about 1.3 mm. This distance can be considered also as the spatial resolution of the approach for deriving strains as the correlation between the strains measured in two different triangle is negligible. The filtering effect of this approach is significant: strains are derived with a resolution of 2.10^{-5}. This performance has been assessed by imaging twice the undeformed specimen and by computing displacement fields from the two undeformed grid images. The derived displacement fields are eventually processed with the piecewise linear functions and strains are derived; 2.10^{-5} is the standard deviation of the derived strain fields.

The fields provided by this approach are discontinuous because they derive from the differentiation of piecewise linear functions (Fig. 6). However, for visualization purpose, continuity can be recovered. The way

Table 1 Constitutive parameters identified with the VFM

	Spec. 1	Spec. 2	Spec. 3	Spec. 4	Spec. 5	Spec. 6
X_1 (GPa)	205	211	215	213	207	210
X_2 (GPa)	55	61	58	64	60	55
X_3 (MPa)	190	187	184	185	184	184
X_4 (GPa)	2.65	2.75	3.16	2.13	2.55	2.81

Table 2 Comparison between the reference values and the identified ones

Reference:	X_1 (GPa)	X_2 (GPa)	X_3 (MPa)	X_4 (GPa)	E (GPa)	ν
Mean	215	60	183	2.46	199	0.28
Coeff. of var. (%)	1.3	6.2	12	20	1.3	6.2
Identified by VFM:						
Mean	210	58	186	2.67	194	0.28
Coeff. of var. (%)	1.7	5.8	1.3	12	1.7	5.8

of recovering strain continuity follows the following stages:

1. Nodal strains are computed as the average of the constant strains of all the neighboring elements;
2. Using the deduced nodal strains, the strain field can be reconstructed using functions $\varphi_k(x, y)$ similarly to the reconstruction of displacement fields in equation (25).

As expected, the strain fields which are eventually obtained (Fig. 7) show that the distribution is heterogeneous already in the elastic range. The largest strains at 2.3 kN (end of elastic domain) are concentrated near the right hand side notch tip. This dissymmetry is caused by the boundary conditions prescribed by our fixture, inducing a slight in-plane moment. Because of this in-plane moment, plastic strains occur very early on the right hand side. Plastic strains occur at 2.3 kN,

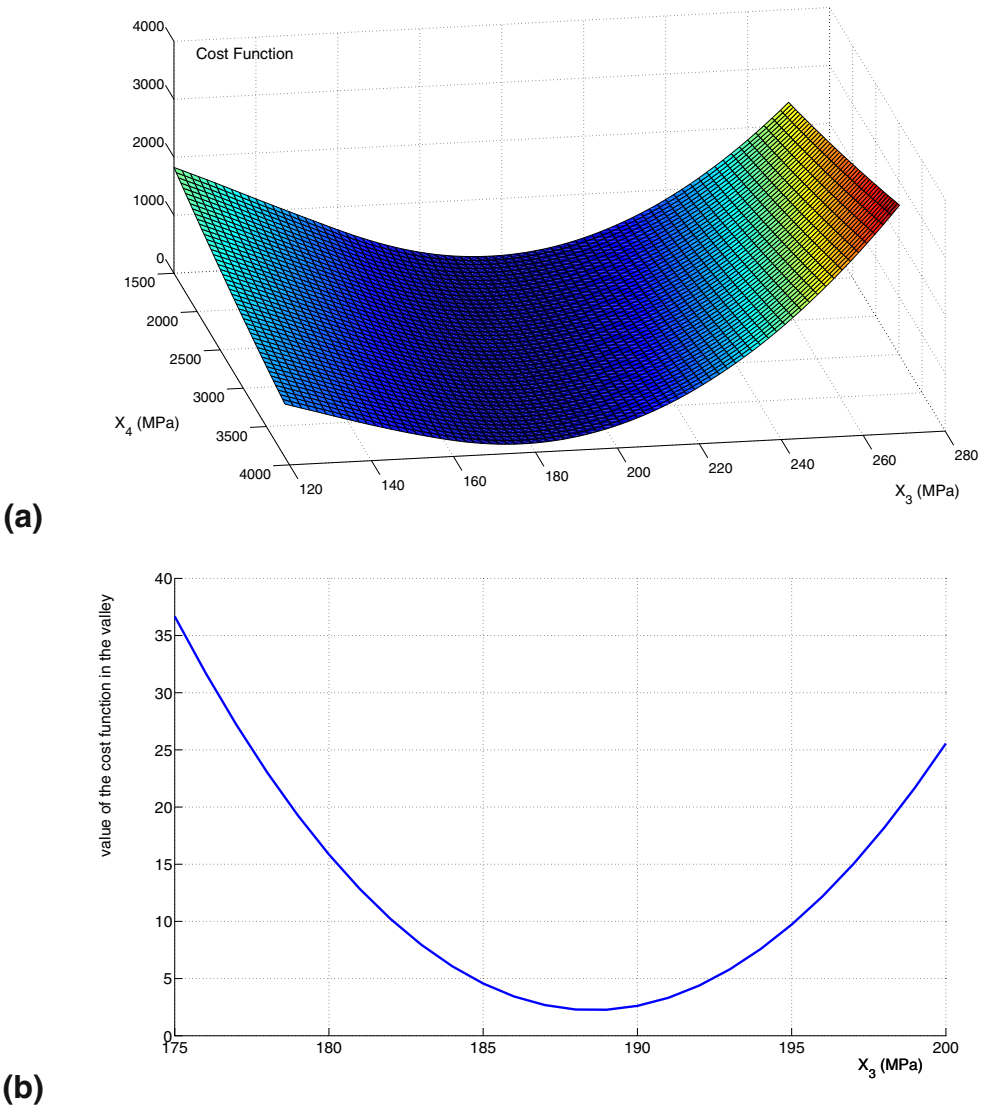

Fig. 8 Shape of the cost function around its minimum. (**a**) 2D plot. (**b**) 1D plot along the line $X_4 = 3,500 - 131(X_3 - 182)$

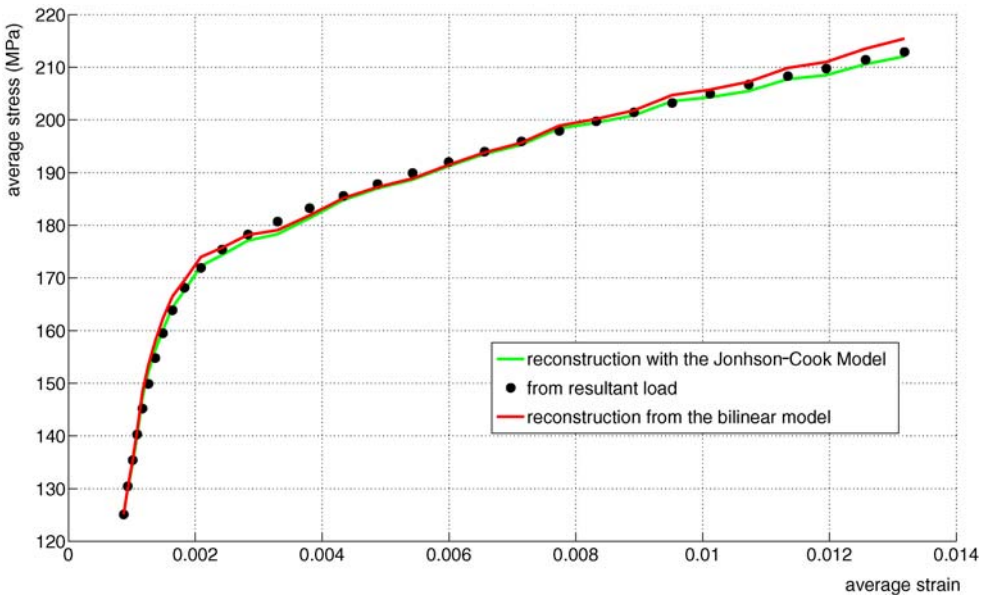

Fig. 9 Comparison between different estimates of the average stress

whereas the average stress in the area of interest is only 40 MPa. They increase very rapidly on the right hand side and then propagate through the whole width of the specimen. Eventually, at 7.88 kN, symmetry between the left hand side and right hand side is nearly recovered.

Similar evolutions of the strain fields were observed in the six tested specimens. This is an interesting example of application for our approach because one has to deal with very localized plasticity and with a heterogeneous distribution of tractions at the boundary of the area of interest.

Identification Results

In each test, the response of the specimen is linear elastic at least up to the seventh time increment. This has been proved by plotting the load curve versus the average strain. In the elastic range, $\dot{\lambda}$ in equation (19) is null, simplifying drastically the way of deriving equations from equation (23) because g does not depend on σ, nor on X_3 and X_4. Considering the cost function in equation (34) but turning m into 7, it is possible to derive directly X_1 and X_2 without any time integration. The results are reported in Table 1.

The two other constants X_3 and X_4 were identified by considering the cost function in equation (34) with $20 \leq i \leq m$. Results are also reported in Table 1.

The average and coefficient of variations of the identified constitutive parameters are compared to the reference parameters in Table 2.

Discussion

The X_1 and X_2 elastic parameters identified with the VFM are stable (coefficients of variation similar to the ones of reference values). If one computes the classical elastic constant E and ν, it can be seen that the Young's modulus is slightly underestimated. The values identified for Poisson's ratio are in very good agreement with the reference values. The underestimation of E may be attributed to data scattering as only 6 specimens were tested for the VFM results and as many for the reference ones.

The plastic parameters are identified using data measured at higher loads ($i \geq 20$). There is a very good agreement between the reference values and the ones identified by the VFM. The coefficients of variation are lower with the VFM than with the standard tests, which may be explained by the averaging effect of processing

Table 3 Constitutive parameters of the Johnson–Cook model identified with the VFM

	Spec. 1	Spec. 2	Spec. 3	Spec. 4	Spec. 5	Spec. 6	average	Coeff. Var.
α (MPa)	183	183	177	184	181	177	181	1.7%
β (MPa)	670	1080	880	1300	1210	1000	1020	22%
η	0.66	0.77	0.68	0.88	0.82	0.72	0.76	11%

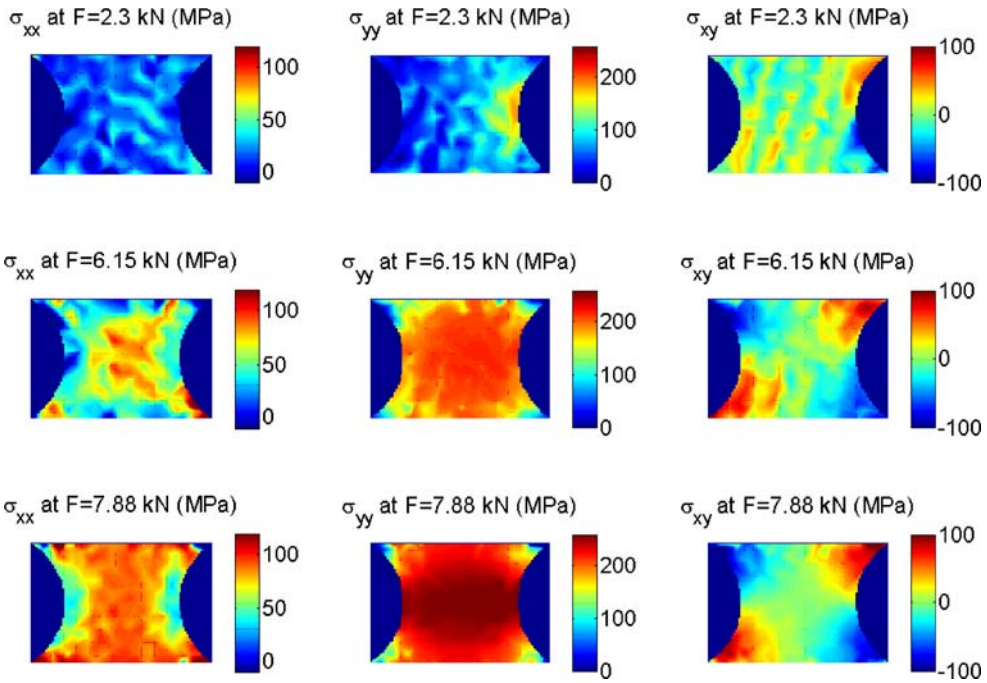

Fig. 10 Distribution of stress components reconstructed from the measurements at different times

fields of measurements instead of strain gages data. Using the average value of the identified parameters, the bilinear model has been used to derive stress/strain curves representing the response of the same material subjected to uniaxial standard tension. The corresponding curve plotted in Fig. 1 shows a very good agreement with the stress/strain curves of the standard tensile tests.

The plastic parameters are identified using an iterative approach for minimizing cost function $\mathcal{F}$ in equation (34). A initial guess for the parameters is required for this approach. Different values were tried out, always yielding the same result within a interval of less than 1%. This is not surprising because the cost function is convex. The shape of the cost function has been plotted in Fig. 8(a). It has a very smooth shape, showing that noise has only a very small effect onto its minimization. It can be noticed that the minimum values are located in a valley between points (182;3,500)

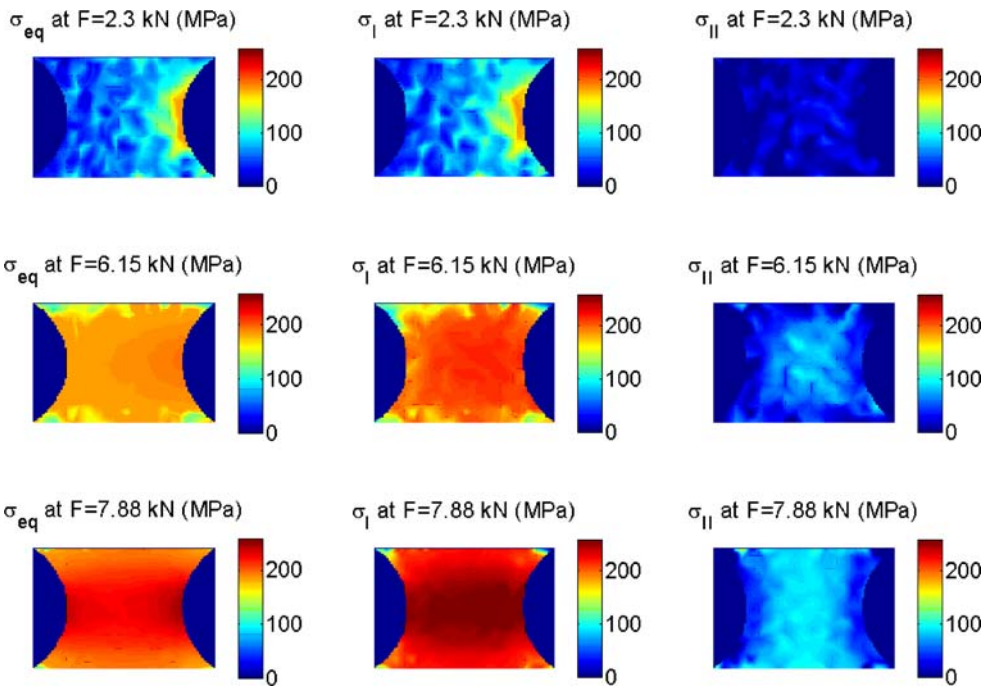

Fig. 11 Distribution of the equivalent Von Mises stress and of the 2D principal stresses reconstructed from the measurements at different times

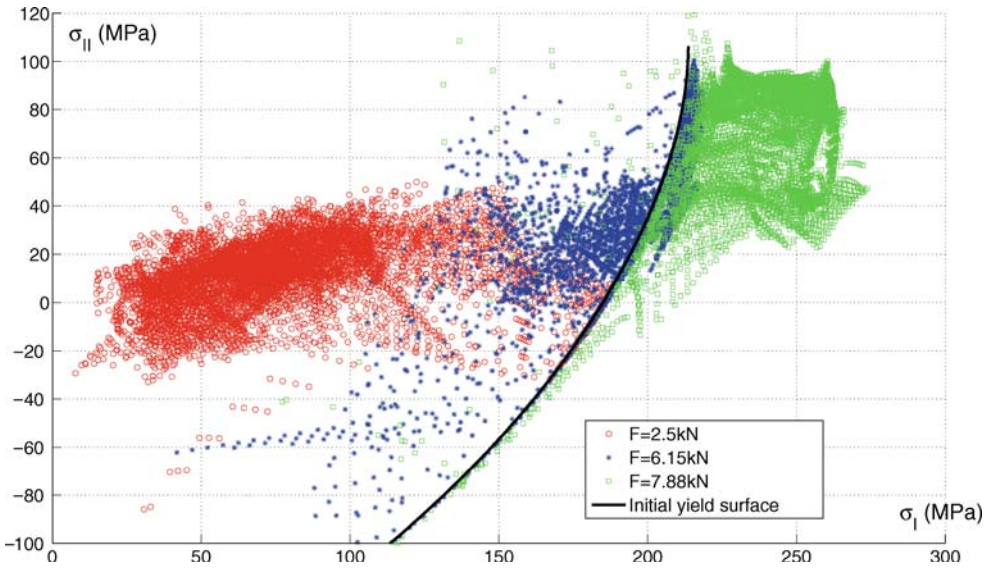

Fig. 12 Graphical display of the principal stresses at different times during the test

and (196;1,650), thus for parameters which are such as: $X_4 = 3,500 - 131(X_3 - 182)$. The existence of this valley does not mean that the cost function has several minima but that the sensitivity to each minimum is different. The sensitivity to X_3 is higher than the sensitivity to X_4: $\partial^2\mathcal{F}/\partial {X_3}^2$=0.22 and $\partial^2\mathcal{F}/\partial {X_4}^2$=0.00035.

If one plots the values of the shape function along the valley [Fig. 8(b)], it can be checked that cost function $\mathcal{F}$ is strictly convex. Accordingly, there is a unique minimum, located at $X_3 = 188$ MPa.

Figure 8(a) shows that the valley is not oriented along one of the axis but with an angle. It means also that both parameters X_3 and X_4 are correlated: $\partial^2\mathcal{F}/\partial X_3 \partial X_4$=0.007. The choice of the virtual fields used in this study has not been optimized, neither to cancel the correlation between parameters X_3 and X_4, nor to balance out the sensitivity of the cost function to each parameters. The choice of the virtual fields in elasto-plasticity was investigated in [14]. Studies are still underway but this is not a critical issue for the present application because of the relatively low number of constitutive parameters to identify.

Actually, only one virtual field was necessary here. It is the one written in equation (21). Only this one was used to build up the cost function. Then, only the first part of the cost function written in equation (34) was used to identify the plastic parameters. Consequently, the cost function figures the quadratic deviation between two estimates of the average stress in the area of interest:

- The first estimate is derived from the measured load: $\bar{\sigma}(t_i) = F_i L/b\,\mathrm{A}$,
- The second estimate is derived from the measured displacement fields:

$$\bar{\sigma}(t_i) = \sum_{n=1}^{N} \frac{\mathrm{A}_n}{\mathrm{A}} \sum_{j=1}^{i-1} g_2\left(\dot{\epsilon}(x_n, y_n, t_j), \sigma(x_n, y_n, t_j), X\right) \tag{35}$$

Both estimates are plotted in Fig. 9 for the identified parameters in one of the tested double-notched specimens. A very good agreement is obtained, showing that the cost function is at its minimum. However, it seems that the slope of the curve derived from the measured loads decreases slightly beyond 0.012, whereas the curve derived from the measured displacement fields with the bilinear model does not. This may indicate that a power function for the hardening model instead of a linear function would be more relevant for higher strains. The relevancy of the Johnson–Cook model did not appear in the standard tensile tests because the specimens were loaded up to a 0.012 strain only (Fig. 1).

The Johnson–Cook model [18] can be written as:

$$\sigma_s = \alpha + \beta p^{\eta} \tag{36}$$

where σ_s is the yield stress at the current state, α and β are two constitutive parameters and η is the hardening sensitivity. The values identified for this model are reported in Table 3. They provide a similar response as the one provided by the bilinear model for strains lower than 0.012. But a better agreement is found between the average reconstructed stress and the one derived from the resultant load for higher strains (Fig. 9). The average value of η is in agreement with the range of possible values for mild steel. Using the average value of the

identified parameters, the Johnson–Cook model has been used to derive stress/strain curves representing the response of the same material subjected to uniaxial standard tension. The corresponding curve plotted in Fig. 1 shows a very good agreement with the bilinear model and with the stress/strain curves of the standard tensile tests.

Using the results provided by our approach, it is also possible to compute the stress components and display their distribution all along the test (Fig. 10). It can be even more interesting to display the distribution of the equivalent Von Mises stress and of the principal stresses (Fig. 11). The principal stresses are computed by diagonalizing the stress tensor at each pixel. Only the two in-plane components are analyzed: σ_I and σ_{II}, because σ_{III} is zero due to the plane-stress assumption. The analysis of principal stresses gives indications about the yield flow in the specimen. For instance, it can be shown from the results displayed in Fig. 11 that the flow follows mainly pure uniaxial tension at the beginning of the test ($F = 2.3$ kN) as the second principal stress is nearly zero everywhere. Afterwards, the flow turns into biaxial tension in the center of the area of interest, with a ratio between the transverse stress and the longitudinal stress of about 0.4. This is even more evident by looking at the graphical display of the principal stresses in Fig. 12. The second principal stress component σ_{II} is plotted versus the first principal stress component σ_I. One data per each triangle is reported at three different times during one of the tests. The initial Von Mises yield surface in this type of graph has the shape of an ellipse. This ellipse appears on the right hand side of the figure. At $F = 2.3$ kN, almost all the triangles have stress states located inside the ellipse, meaning that plasticity has not occurred yet. At $F = 7.88$ kN, almost all the area of interest of the specimen has yielded, and a significant second principal stress has appeared, meaning that the yield flow has changed during the test. It is interesting to notice that many points at $F = 6.15$ kN are located on the ellipse of the initial Von Mises yield surface. The reason for that is that plasticity occurs first on the right hand side of the specimen and then propagates towards the left hand side without hardening. Once plasticity has occurred on the right hand side, the in-plane bending which was significant at the beginning of the test tends to fade away. Consequently, the stress can only increase significantly and the material can only harden when the whole cross section has yielded. This is what has occurred at $F = 7.88$ kN where most of the points are outside the initial Von Mises yield surface.

The transition from localized plasticity to global plasticity is an interesting aspect because it means that our approach is able to deal with different flow directions in the same test, i.e. non proportional loading. It is promising for characterizing more complicated materials with an anisotropic behavior that could be described by Hill's yield function instead of Von Mises yield function for instance, and with kinematic hardening combined to isotropic hardening. The choice of relevant virtual fields may become a critical issue when dealing with such anisotropic constitutive equations as one would have to filter out the contribution of a larger number of parameters into the global response of the specimen. A study is currently underway for solving this issue.

Conclusion

The present study has shown that it is possible to identify elasto-plastic parameters and to reconstruct stress fields from full-field displacement measurements without performing any finite element computations. Even for tests giving rise to heterogeneous stress fields and to complicated yield flows, stress fields are derived directly from the measured data and updated until the principle of virtual work is satisfied. Applied onto experimental data, our approach provided constitutive parameters which were in agreement with their reference counterparts, both in the elastic and plastic domains. Moreover, it was proved that the identification of the constitutive parameters is much faster with our approach than with classical finite element model updating.

The experimental results were obtained for simple elasto-plastic constitutive equations (only four or five parameters) and simple virtual fields were used. The choice of virtual fields needs to be optimized for more sophisticated constitutive equations. Indeed, the approach is obviously to be extended to conditions which are closer to the reality of forming processes: anisotropy, larger strains, material heterogeneities, higher strain rates. Regarding the latter, developments for dealing with viscoplastic models are already underway [27].

Acknowledgements The authors are grateful to the "Conseil Régional de Champagne Ardenne" for its financial support to this study through the PhD grant of Yannick Pannier, as well as the Agence Nationale de la Recherche (ANR, France) through the PHOTOFIT programme (Grant ANR-05-BLAN-0327-01).

References

1. Laws V (1981) Derivation of the tensile stress-strain curve from bending data. J Mater Sci 16:1299–1304.
2. Mayville RA, Finnie I (1982) Uniaxial stress-strain curves from a bending test. Exp Mech 22:197–201.

3. Brunet M, Morestin F, Godereaux S (2001) Nonlinear kinematic hardening identification for anisotropic sheet metals with bending-unbending tests. J Eng Mater Technol 123: 378–383.
4. Zhao KM (2004) Inverse estimation of material properties for sheet metals. Commun Numer Methods Eng 20: 105–118.
5. Mahnken R, Stein E (1994) The identification of parameters for visco-plastic models via finite-elements methods and gradient methods. Model Simulation Mater Sci Eng 2:597–616.
6. Mahnken R, Stein E (1996) A unified approach for parameter identification of inelastic material models in the frame of the finite element method. Comput Methods Appl Mech Eng 136:225–258.
7. Meuwissen MHH (1998) An inverse method for the mechanical characterisation of metals. PhD thesis, Eindhoven Technical University.
8. Meuwissen MHH, Oomens CWJ, Baaijens FPT, Petterson R, Janssen JD (1998) Determination of the elasto-plastic properties of aluminium using a mixed numerical-experimental method. J Mater Process Technol 75:204–211.
9. Okada H, Fukui Y, Kumazawa N (1999) An inverse analysis determining the elastic-plastic stress-strain relationship using nonlinear sensitivities. Comput Model Simulation Eng 4(3):176–185.
10. Hoc T, Crépin J, Gélébart L, Zaoui A (2003) A procedure for identifying the plastic behaviour of single crystals from the local response of polycrystals. Acta Materialia 51: 5477–5488.
11. Kajberg J, Lindkvist G (2004) Characterization of materials subjected to large strains by inverse modelling based on in-plane displacement fields. Int J Solids Struct 41: 3439–3459.
12. Cooreman S, Lecompte D, Sol H, Vantomme J, Debruyne D (2007) Elasto-plastic material parameter identification by inverse methods: Calculation of the sensitivity matrix. Int J Solids Struct 44(13):4329–4341.
13. Geng L, Shen Y, Wagoner RH (2002) Anisotropic hardening equations derived from reverse-bend testing. Int J Plasticity 18(5-6):743–767.
14. Grédiac M, Pierron F (2006) Applying the virtual field method to the identification of elasto-plastic constitutive parameters. Int J Plasticity 22(4):602–627.
15. Grédiac M, Pierron F, Avril S, Toussaint E (2006) The virtual fields method for extractiong constitutive parameters from full-field measurements: a review. Strain 42:233–253.
16. Pannier Y, Avril S, Rotinat R, Pierron R (2006) Identification of elasto-plastic constitutive parameters from statically undetermined tests using the virtual fields method. Exp Mech 46(6):735–755.
17. Sutton MA, Deng X, Liu J, Yang L (1996) Determination of elastic–plastic stresses and strains from measured surface strain data. Exp Mech 36(2):99–112.
18. Lemaître J, Chaboche J-L (1990) Mechanics of solid materials. Cambridge University Press, Cambridge, UK.
19. Grédiac M, Toussaint E, Pierron F (2002) Special virtual fields for the direct determination of material parameters with the virtual fields method. 1–Principle and definition. Int J Solids Struct 39(10):2691–2705.
20. Grédiac M, Toussaint E, Pierron F (2002) Special virtual fields for the direct determination of material parameters with the virtual fields method. 2–Application to in-plane properties. Int J Solids Struct 39(10):2707–2730.
21. Chapelle D, Darrieulat M (2003) The occurence of shear banding in a millimeter scale (123)[634] grain of an al-4.5% Mg alloy during plane strain compression. Mater Sci Eng A 347(1-2):32–41.
22. Avril S, Pierron F (2007) General framework for the identification of constitutive parameters from full-field measurements in linear elasticity. Int J Solids Struct 44(14-15): 4978–5002.
23. Avril S, Grédiac M, Pierron F (2004) Sensitivity of the virtual fields method to noisy data. Comput Mech 34(6):439–452.
24. Feng Z, Rowlands RE (1991) Smoothing finite-element and experimental hybrid technique for stress analyzing composites. Computer Struct 6:631–639.
25. Piro J-L, Grédiac M (2004) Producing and transferring low-spatial-frequency grids for measuring displacement fields with moiré and grid methods. Experimental Techniques 28(4):23–26.
26. Surrel Y (1996) Design of algorithms for phase measurements by the use of phase-stepping. Appl Optic 35(1):51–60.
27. Avril S, Pierron F, Yan J, Sutton M (2007) Identification of strain-rate sensitivity with the virtual fields method. In: Gdoutos E (ed) Proceedings of ICEM13, Alexandoupolis, Greece.